# On the formation of geophysical and planetary zonal flows by near-resonant wave interactions

## YOUNGSUK LEE[1] AND LESLIE M. SMITH[2]

[1]Department of Mathematics, Simon Fraser University, Burnaby, BC V5A 1S6, Canada
[2]Departments of Mathematics and Engineering Physics, University of Wisconsin, Madison, WI 53706, USA

Numerical simulations on a $\beta$-plane are used to further understand the formation of zonal flows from small-scale fluctuations. The dynamics of 'reduced models' are computed by restricting the nonlinear term to include a subset of triad interactions in Fourier space. Reduced models of near-resonant triads are considered, as well as the complement set of non-resonant triads. At moderately small values of the Rhines number, near-resonant triad interactions are shown to be responsible for the generation of large-scale zonal flows from small-scale random forcing. Without large-scale drag, both the full system and the reduced model of near resonances produce asymmetry between eastward and westward jets, in favour of stronger westward jets. When large-scale drag is included, the long-time asymmetry is reversed in the full system, with eastward jets that are thinner and stronger than westward jets. Then the reduced model of near resonances exhibits a weaker asymmetry, but there are nevertheless more eastward jets stronger than a threshold value.

## 1. Introduction

The two-dimensional $\beta$-plane equation is one of the simplest models of geophysical and planetary fluid flow, and has been studied in depth since the pioneering work by Rhines (1975). It is often used to model the mid-latitude dynamics of zonal flows and vortices such as the North American jet stream, the Gulf Stream and the Jovian Great Red Spot (e.g. Williams 1978; Sommeria, Meyers & Swinney 1988; Marcus, Kundu & Lee 2000; Afanasyev & Wells 2005). Within the context of a two-layer model, Rhines (1979) showed how energy is converted from baroclinic to barotropic flow, followed by a cascade to large scales, lending credence to barotropic analyses such as flow on the $\beta$-plane.

Dynamics on the $\beta$-plane involve the complex interaction of turbulence and dispersive waves, with dispersion relation proportional to $k_x/(k_x^2 + k_y^2)$, where $(x, y)$ are the zonal and meridional directions, respectively. The dispersion relation indicates that zonal modes with $k_x = 0$ are 'slow', that is, they have zero frequency. Many numerical simulations of $\beta$-plane flows have shown that large-scale zonal flows with $k_x = 0$ are spontaneously generated from isotropic small-scale forcing (Rhines 1975; Vallis & Maltrud 1993; Chekhlov *et al.* 1996; Smith & Waleffe 1999; Marcus *et al.* 2000; Huang, Galperin & Sukoriansky 2001; Manfroi & Young 2002; Sukoriansky, Galperin & Dikovskaya 2002; Okuno & Masuda 2003; Danilov & Gryanik 2004; Danilov & Gurarie 2004; Smith 2004). A similar phenomenon is seen in simulations of two-dimensional flow on the surface of a rotating sphere (Nozawa & Yoden 1997;

Williams 1978; Huang & Robinson 1998; Huang *et al.* 2001). Random forcing has been proposed to model both the baroclinic instability (Williams 1978) and small-scale convection (Gierasch *et al.* 2000; Ingersoll *et al.* 2000). Our purpose is to investigate which specific wave interactions are responsible for the generation of large-scale zonal flows from random small-scale isotropic fluctuations.

In fact, the formation of large-scale zonal flows and vortices from small-scale fluctuations appears to be a universal feature of rotating and stratified flows, even in three dimensions (Hopfinger, Browand & Gagne 1982; Smith 2001; Lollini & Godeferd 1999; Smith & Waleffe 1999, 2002; Longhetto *et al.* 2002; Baroud *et al.* 2003). In search of a generic mechanism, we follow the procedure introduced in Smith & Lee (2005) to study subsets of triad interactions in Fourier space. Since nonlinear coupling between scales occurs through a quadratic nonlinearity, that coupling is achieved through three-wave interactions when the flow is represented as a superposition of Fourier modes. For three-dimensional flow in a rotating frame with constant Coriolis parameter (constant rotation rate), Smith & Lee (2005) showed that a reduced model including only near-resonant triad interactions reproduced all the important features of the full simulations with random forcing at small scales, namely, (i) efficient transfer of energy from small-scale fast waves to slow large-scale coherent vortical columns, (ii) approximate scaling of the large-scale energy spectrum $E(k) \propto k^{-3}$, and (iii) strong asymmetry between cyclones and anticyclones in favour of cyclones. Here we consider the two-dimensional $\beta$-plane equation with a linear term to model the latitude variation of the Coriolis parameter.

A non-dimensional Rhines number $Rh$ may be defined for the $\beta$-plane system as the ratio of linear and nonlinear time scales. Then, when the equations are non-dimensionalized based on the nonlinear time scale and assuming small $Rh$, linear effects are dominant for times of $O(Rh)$, exactly resonant triad interactions become important for times $O(1)$, and nearly resonant triad interactions contribute to the dynamics on longer time scales $O(1/Rh)$ (Newell 1969). Exactly resonant triads satisfy the condition $\sigma(\boldsymbol{k}) + \sigma(\boldsymbol{p}) + \sigma(\boldsymbol{q}) = 0$ for an interaction between modes with wavevectors $\boldsymbol{k}$, $\boldsymbol{p}$ and $\boldsymbol{q}$, where $\sigma(\boldsymbol{k})$ is the wave frequency given by the dispersion relation. Nearly resonant triads are defined by $\sigma(\boldsymbol{k}) + \sigma(\boldsymbol{p}) + \sigma(\boldsymbol{q}) = O(Rh)$. Thus for any finite, small value of $Rh$, one expects to see the effects of near-resonant interactions on long time scales $O(1/Rh)$. It is of theoretical interest that exactly resonant triad interactions cannot transfer energy from fast waves to zonal flows on the $\beta$-plane (Longuet-Higgins & Gill 1967). This means that higher-order effects such as nearly resonant triads and/or resonant quartets (Newell 1969) must be responsible for the formation of zonal flows from small-scale fluctuations. Herein, we often abbreviate 'near-resonant triad interactions' by 'near resonances'.

With characteristic length scale $L$ and nonlinear time scale $L/U$, the Rhines number for the $\beta$-plane equation is $Rh = U/(L^2\beta)$, where $\beta$ has dimensions of $(\text{length} \times \text{time})^{-1}$. Using a large-scale wind speed of $U \approx 10 \text{ m s}^{-1}$, a characteristic length scale $L \approx 1000 \text{ km}$ and a mid-latitude $\beta = O(10^{-13}) \text{ cm}^{-1} \text{ s}^{-1}$, (Pedlosky 1986, chap. 6) estimates atmospheric values of $Rh \approx 1$. The values $U \approx 5 \text{ cm s}^{-1}$ and $L \approx 100 \text{ km}$, which are more typical of the western Atlantic, give $Rh \approx 0.5$.

For resolution $512^2$ Fourier modes and forcing at wavenumber $100 \leqslant k \leqslant 105$, Chekhlov *et al.* (1996) considered values $Rh = \infty$ ($\beta = 0$), $Rh = 2.63$ and $Rh = 0.47$. The limit $Rh \to \infty$ tends toward isotropic two-dimensional flow. The Rhines number was defined as $Rh = (\varepsilon_f k_f^5)^{1/3}/\beta$, with characteristic length $L = 1/k_f$ and nonlinear time scale $L/U = (\varepsilon_f k_f^2)^{-1/3}$ determined by the peak wavenumber $k_f$ and the energy input rate $\varepsilon_f$ of the force. For $Rh = 2.63$, Chekhlov *et al.* (1996) found strong

zonal/meridional anisotropy at long times and for wavenumbers $k < k_\beta = 56$, where $k_\beta \equiv (\beta^3/\varepsilon)^{1/5}$. For the smaller $Rh = 0.47$, dominance of zonal flows emerged faster, and for wavenumbers $k < k_\beta = 158$ (for all wavenumbers smaller than the forced wavenumbers). Thus for our simulations, we choose the physically relevant value $Rh \approx 0.5$, which produces strong anisotropy at all wavenumbers smaller than the forced wavenumbers (e.g. we use $k_f = 75$ in $384^2$). Significantly smaller values of $Rh$ would presumably require higher resolutions in order to capture adequately the near-resonant triads with $\sigma(\boldsymbol{k}) + \sigma(\boldsymbol{p}) + \sigma(\boldsymbol{q}) = O(Rh)$ (Pushkarev & Zakharov 2000; Connaughton, Nazarenko & Pushkarev 2001; Smith & Lee 2005).

We focus on the role of near-resonant triad interactions in the generation of strongly anisotropic large-scale zonal flows. We are interested in the formation of zonal flows, as well as their characteristics in a state of roughly constant energy. Thus we present results for (i) time-developing dynamics without large-scale dissipation, and (ii) the approach to a state of constant energy with a linear drag term to mimic Ekman boundary-layer drag (Salmon 1998). For case (i) without large-scale damping, we follow the time-developing dynamics until well before the energy in the lowest available wavenumber $k = 1$ exceeds a value consistent with large-scale energy spectral scaling $E(k) \propto k^{-5}$. The scaling $E(k) \propto k^{-5}$ is observed at large scales in simulations of strongly anisotropic $\beta$-plane flow and two-dimensional flow on a rotating sphere, before significant energy accumulation in the characteristic scale defined by the large-scale dissipation parameters (e.g. Chekhlov *et al.* 1996; Smith & Waleffe 1999; Marcus *et al.* 2000; Huang *et al.* 2001; Manfroi & Young 2002; Sukoriansky *et al.* 2002; Okuno & Masuda 2003; Smith 2004). Observations on Jupiter and Saturn show a zonal spectrum scaling as $k^{-5}$ in the range of wavenumbers not affected by large-scale friction (Galperin *et al.* 2001). For case (ii) with large-scale linear damping, we allow the flow to approach a state of constant energy (see figure 2*b*). At much later times (beyond the scope of our work), Danilov & Gryanik (2004) and Danilov & Gurarie (2004) showed that the the large-scale energy spectrum develops distinct peaks at the wavenumbers corresponding to the dissipation scale and its harmonics (see also Smith & Yakhot 1994).

It is important to keep in mind that the physical-space form of the nonlinear term for a reduced model is not known. Thus, to study near-resonant triads in isolation, fully spectral simulations rather than pseudospectral simulations are necessary, increasing the time costs and limiting the resolution of the reduced-model calculations. To compare reduced-model and full simulations without linear drag, we use a resolution of $384^2$ Fourier modes and forcing in the range $67.5 \leqslant k \leqslant 82.5$; for longer-time runs with large-scale dissipation, we use $256^2$ Fourier modes and forcing in the range $45 \leqslant k \leqslant 55$. We find that near-resonant triad interactions alone are more efficient at creating large-scale zonal flows than the full set of triad interactions. In contrast, non-resonant triad interactions do not produce strong zonal/meridional anisotropy.

For three-dimensional rotation at moderate Rossby number $Ro \approx 0.1$, vortical columns develop from small-scale random forcing. During development of the vortices and without large-scale damping, the full simulations show strong cyclone/anticyclone asymmetry in favour of cyclones, and this asymmetry was reproduced by the reduced model of near-resonant triads (Smith & Lee 2005). The Rossby number in three-dimensional rotation is the counterpart to the Rhines number for $\beta$-plane flow, measuring the ratio of linear and nonlinear time scales. During the development of zonal flows from-small scale fluctuations on the $\beta$-plane, simulations of the full system and of near resonances also share an asymmetry between westward and eastward jets. In this case, larger amplitudes are associated with the westward jets,

and simulations of near resonances alone are shown to amplify the asymmetry. When large-scale damping is added, so that the flow approaches a state of constant energy, then the eastward jets have higher velocities and are thinner in extent, for both (full) $\beta$-plane flow and flow on a rotating sphere (see e.g. Nozawa & Yoden 1997; Danilov & Gryanik 2004, and our figure 8). In addition, the zonally averaged vorticity exhibits a characteristic 'sawtooth' pattern (see e.g. Danilov & Gryanik 2004, and our figure 8). In our simulations of near-resonances only, these features are present, but somewhat obscured by a secondary flow structure corresponding to a secondary peak in the energy spectrum (at higher wavenumber than the primary peak associated with the large-scale dissipation wavenumber). Apparently, non-resonant interactions contribute to produce the signature associated with the full flow by suppressing this secondary structure. However, non-resonances alone do not produce strongly zonal flows, either with or without large-scale drag.

Our work is complementary to statistical approaches such as the closure theory of Holloway & Hendershott (1977) and weak turbulence theory (see e.g. Reznik & Soomere 1983; Balk 1991, 2005; Balk, Nazarenko & Zakharov 1991, and references therein). Similar to the present work, the closure of Holloway & Hendershott (1977) describes the transition from pure turbulence ($Rh \to \infty$) to wave-dominated dynamics ($Rh \to 0$) by including near-resonant interactions at moderate values of the Rhines number, but within a statistical framework describing the covariance of the vertical vorticity. In the weak turbulence regime for $Rh \to 0$, Reznik & Soomere (1983) showed that zonal flows are thermodynamical equilibrium solutions to the kinetic equations. Later, Balk (1991, 2005) and Balk *et al.* (1991) linked the formation of large-scale zonal flows to the existence of a new invariant conserved by exact three-wave resonances. As shown by Longuet-Higgins & Gill (1967), for an exact resonance involving one zonal mode and two wave modes, there is no energy transfer to the zonal mode, which acts only as a catalyst for energy transfer between the wave modes. However, near resonances should approximately conserve the new invariant, and we show that near resonances generate strongly zonal flows at moderately small Rhines number. The approach adopted here, to study directly the dynamics of the near resonances and other reduced models, has the advantage that it allows for investigation of the asymmetry between eastward and westward zonal flows, which asymmetry is not included in the description provided by statistical closure or weak turbulence theory.

The remainder of the paper is organized as follows. In §2, we introduce the governing equations and explain what is meant by a 'reduced model'. Section 3 describes the procedure to calculate the nonlinearity of a reduced model in Fourier space. The results of numerical simulations are presented in § 4. Conclusions and discussion are contained in § 5.

## 2. Flow on the $\beta$-plane

### 2.1. *The governing equations and properties*

The $\beta$-plane equation may be written in non-dimensional form as

$$\partial_t \zeta + J(\nabla^{-2}\zeta, \zeta) + \frac{1}{Rh}\partial_x \nabla^{-2}\zeta = \frac{1}{Re}\nabla^2\zeta - \Lambda\zeta + f, \qquad (2.1)$$

where $\zeta = v_x - u_y$ is the vorticity, $f$ is an external force, $J(g, h) = g_x h_y - g_y h_x$ is the Jacobian, $Re = UL/\nu$ is the Reynolds number, $Rh = U/(\beta L^2)$ is the Rhines number, $\Lambda = rU/L$ is a non-dimensional drag coefficient, $U$ and $L$ are characteristic velocity

and length scales, $r$ is the (dimensional) drag coefficient, and the parameter $\beta$ is the linear variation of the Coriolis parameter (see e.g. Pedlosky 1986; Salmon 1998).

In the absence of external forcing and in a periodic domain, the inviscid ($Re \to \infty$, $\Lambda \to 0$), linear limit of (2.1) has wave solutions of the form

$$\zeta(\boldsymbol{x}, t; \boldsymbol{k}) = \exp\left[i\left(\boldsymbol{k} \cdot \boldsymbol{x} - \sigma(\boldsymbol{k})\frac{t}{Rh}\right)\right] + \text{c.c.}, \quad \boldsymbol{k} = (k_x, k_y), \quad (2.2)$$

where c.c. denotes a complex conjugate and the dispersion relation is

$$\sigma(\boldsymbol{k}) = -\frac{k_x}{k^2}. \quad (2.3)$$

The solution $\zeta(\boldsymbol{x}, t)$ may be represented as a superposition of linear waves (2.2), formally written as

$$\zeta(\boldsymbol{x}, t) = \sum_{\boldsymbol{k}} b(t; \boldsymbol{k}) \exp\left[i\left(\boldsymbol{k} \cdot \boldsymbol{x} - \sigma(\boldsymbol{k})\frac{t}{Rh}\right)\right], \quad (2.4)$$

with reality condition $b(t; \boldsymbol{k}) = b^*(t; -\boldsymbol{k})$. Substitution of (2.4) into (2.1) yields

$$\left(\frac{\partial}{\partial t} + \frac{1}{Re}k^2\right)b(t; \boldsymbol{k}) = \sum_{\triangle_{k,p,q}} C_{kpq} b^*(t; \boldsymbol{p}) b^*(t; \boldsymbol{q}) \exp\left[i(\sigma(\boldsymbol{k}) + \sigma(\boldsymbol{p}) + \sigma(\boldsymbol{q}))\frac{t}{Rh}\right], \quad (2.5)$$

where the sum is over all triads $\triangle_{k,p,q}$ with $\boldsymbol{k} + \boldsymbol{p} + \boldsymbol{q} = \boldsymbol{0}$. Relation (2.3) allows resonant triad interactions with

$$\boldsymbol{k} + \boldsymbol{p} + \boldsymbol{q} = \boldsymbol{0}, \quad \sigma(\boldsymbol{k}) + \sigma(\boldsymbol{p}) + \sigma(\boldsymbol{q}) = 0, \quad (2.6)$$

and the slow modes with $k_x = 0$ cannot gain or lose energy directly by resonant triad interactions (Longuet-Higgins & Gill 1967). The real-valued coefficients $C_{kpq}$ are given by

$$C_{kpq} = (q^{-2} - p^{-2})(\boldsymbol{p} \times \boldsymbol{q}) \cdot \hat{\boldsymbol{z}} \quad (2.7)$$

and they satisfy

$$\left.\begin{aligned} C_{kpq} + C_{pqk} + C_{qkp} &= \boldsymbol{0}, \\ k^{-2}C_{kpq} + p^{-2}C_{pqk} + q^{-2}C_{qkp} &= \boldsymbol{0}, \end{aligned}\right\} \quad (2.8)$$

as can be deduced, respectively, from energy and enstrophy conservation by triad interactions.

Simulations of flow on the $\beta$-plane with isotropic forcing and hyperviscosity at small scales show strong energy transfer into large-scale zonal flows (Vallis & Maltrud 1993; Chekhlov *et al.* 1996; Smith & Waleffe 1999; Marcus *et al.* 2000; Huang *et al.* 2001; Manfroi & Young 2002; Sukoriansky *et al.* 2002; Okuno & Masuda 2003; Danilov & Gryanik 2004; Danilov & Gurarie 2004; Smith 2004). As noted above, transfer into zonal flows cannot be the direct result of resonant triad interactions (2.6). Thus we investigate near-resonant triads, with the sum of frequencies $O(Rh)$ rather than zero. Before energy accumulation in the large-scale damping wavenumber, or in the lowest available wavenumber for runs without large-scale damping, the large-scale energy spectrum exhibits the scaling $E(k) \propto \beta^2 k^{-5}$ as predicted by Rhines (1975) (see figure 3 and e.g. Chekhlov *et al.* 1996). The original argument for the $k^{-5}$ scaling by Rhines (1975) was the tendency of the local Rhines number (the wave steepness) $U/(\beta L^2)$ to approach unity.

## 2.2. Reduced models

To study the role of near-resonant triad interactions in the generation of large-scale zonal flows, we considered 'reduced models' (see also Smith & Lee 2005). In numerical simulations with finite resolution, the sum of the nonlinear interactions in (2.5) is replaced by the sum over $\mathscr{I}_F$, where $\mathscr{I}_F$ is the finite set of all triad interactions in the numerical domain. Generally, given a proper subset $\mathscr{I}$ of triad interactions in $\mathscr{I}_F$, the analogue of (2.5) obtained by the sum of nonlinear interactions over $\mathscr{I}$

$$\left(\frac{\partial}{\partial t} + \frac{1}{Re}k^2\right)b(t;\boldsymbol{k}) = \sum_{\mathscr{I}} C_{\boldsymbol{kpq}}b^*(t;\boldsymbol{p})b^*(t;\boldsymbol{q})\exp\left[\mathrm{i}(\sigma(\boldsymbol{k})+\sigma(\boldsymbol{p})+\sigma(\boldsymbol{q}))\frac{t}{Rh}\right], \quad (2.9)$$

is here referred to as a reduced model.

The role of near-resonant triad interactions is the main focus of this paper, and $\mathscr{I}_R(\epsilon; Rh)$ denotes the set of all triad interactions satisfying

$$|\sigma(\boldsymbol{k}) + \sigma(\boldsymbol{p}) + \sigma(\boldsymbol{q})| \leqslant \epsilon\, Rh \quad (2.10)$$

for positive $\epsilon = O(1)$. Likewise, the reduced model of non-resonances includes the complement of (2.10), with $\leqslant$ replaced by $>$, denoted by $\mathscr{I}_N(\epsilon; Rh)$. Note that in any reduced model, we keep all wave amplitudes (all the $b(t;\boldsymbol{k})$), but include a subset $\mathscr{I}$ of triad interactions from $\mathscr{I}_F$.

The quadratic nonlinearity in the discretized equations with nonlinear term $NL(\mathscr{I}_F)$ can be computed efficiently by the standard pseudo-spectral technique using fast Fourier transforms (FFTs) with, e.g. the 2/3 rule for dealiasing (e.g. Boyd 2001; Canuto *et al.* 1988). However, when the nonlinear term is modified to include only a subset of triad interactions, the modified nonlinearity must be calculated directly in spectral space. Both time and storage costs for such direct calculations are more expensive, and thus numerical simulations of the reduced models are restricted to lower resolutions (our calculations use $384^2$ or $256^2$ Fourier modes). (Computational time is the limiting factor. However, storage costs are also high if one saves the interaction coefficients $C_{\boldsymbol{kpq}}$.) In the next section, we provide more specifics for our computations of reduced dynamics. The reader who is not interested in such details should proceed to §4.

## 3. Direct calculation of the nonlinear interactions in wave space

Since the physical space form of the modified nonlinearity is not known for a reduced model, that modified nonlinearity is calculated directly in Fourier space. The procedure for a quadratic nonlinearity is described in Smith & Lee (2005), and is repeated here for completeness.

For a reduced model associated with $\mathscr{I}$, the governing equation (2.9) can be written as

$$\left(\frac{\partial}{\partial t} + \frac{\mathrm{i}\sigma(\boldsymbol{k})}{Rh} + \frac{k^2}{Re}\right)a(\boldsymbol{k}) = \sum_{\mathscr{I}} n(\boldsymbol{k};\boldsymbol{p},\boldsymbol{q}), \quad n(\boldsymbol{k};\boldsymbol{p},\boldsymbol{q}) = C_{\boldsymbol{kpq}}a^*(\boldsymbol{p})a^*(\boldsymbol{q}), \quad (3.1)$$

where $a(\boldsymbol{k}) = b(t;\boldsymbol{k})\exp(-\mathrm{i}\sigma(\boldsymbol{k})t/Rh)$ includes the phase factor. The expression $n(\boldsymbol{k};\boldsymbol{p},\boldsymbol{q})$ is the nonlinear contribution to $\boldsymbol{k}$ through the triad interaction between $\boldsymbol{k}$, $\boldsymbol{p}$ and $\boldsymbol{q}$. It is straightforward to check (i) $C_{\boldsymbol{kpq}} = C_{-\boldsymbol{k},-\boldsymbol{p},-\boldsymbol{q}}$, (ii) $C_{\boldsymbol{kpq}} = C_{\boldsymbol{kqp}}$ (so that $n(\boldsymbol{k};\boldsymbol{p},\boldsymbol{q}) = n(\boldsymbol{k};\boldsymbol{q},\boldsymbol{p})$), and (iii) $C_{\boldsymbol{kpq}} = 0$ if $\boldsymbol{k}$, $\boldsymbol{p}$ and $\boldsymbol{q}$ are collinear. Condition (iii) allows the sum in (3.1) to be restricted to non-collinear triads. Here, we are concerned with the direct calculation of the nonlinear interactions in (3.1).
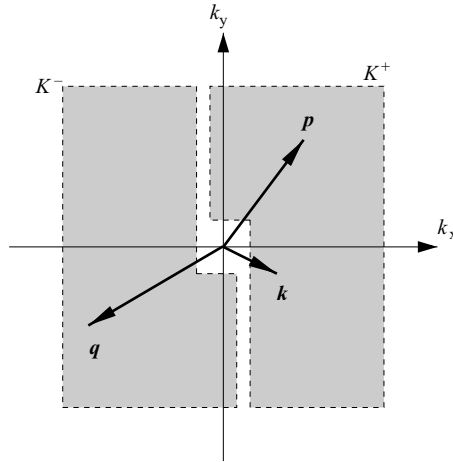
FIGURE 1. $K^+$ is the domain in Fourier space for the pseudospectral method. The triad $\triangle_{kpq}$ is in $T^+$ with $\boldsymbol{k} < \boldsymbol{p}$.

For the pseudospectral method over a two-dimensional periodic square, the domain of wavevectors for an isotropic grid in Fourier space is

$$K^+ = \{\boldsymbol{k} = (j_x, j_y)\Delta k\} \begin{cases} \text{either} & j_x = 0, \quad j_y = 1, 2, \cdots, M, \\ \text{or} & j_x = 1, 2, \cdots, M, \quad j_y = -M, -M+1, \cdots, M, \end{cases} \quad (3.2)$$

where $\Delta k$ is the distance between two adjacent wavevectors and $M$ is a positive integer (Boyd 2001; Canuto *et al.* 1988). The region $K^+$ is the right-hand grey area in figure 1, and $K^- = -K^+ = \{\boldsymbol{k} : -\boldsymbol{k} \in K^+\}$. As a consequence of the reality conditions on $a(\boldsymbol{k})$ and $C_{kpq}$, only information in $K^+$ is needed to construct the wave field over the entire square $K^+ \cup K^-$. Note that $M$ is usually chosen as one third of the resolution size to avoid aliasing by using the so-called 2/3 rule.

Let $T^+$ be the set of all non-collinear triads with two wavevectors in $K^+$ and the remaining wavevector in $K^-$. (We use $T$ for a set of triads, and $\mathscr{I}$ for a set of triad interactions. However, since there is one triad interaction for a given triad, $T$ and $\mathscr{I}$ are essentially the same. This is not the case for rotating flows in Smith & Lee 2005). For example, the triad in figure 1 is in $T^+$ because $\boldsymbol{k}, \boldsymbol{p} \in K^+$ and $\boldsymbol{q} \in K^-$. Let $T^-$ be the set of triads whose Fourier conjugate is in $T^+$: $T^- = \{\triangle_{kpq} : \triangle_{-k,-p,-q} \in T^+\}$. So, any triad in $T^-$ has two wavevectors in $K^-$ and the remaining wavevector in $K^+$. Thus, any non-collinear triad is in either $T^+$ or $T^-$.

To describe a numerical procedure to compute the nonlinear interactions in (3.1), let $T$ be the set of triad interactions associated with $\mathscr{I}$ ($T$ is a subset of $T^+ \cup T^-$). For fixed triad $\triangle_{kpq}$ in $T \cap T^+$, without loss of generality, $\boldsymbol{k}$ and $\boldsymbol{p}$ are in $K^+$ and $\boldsymbol{q}$ is in $K^-$. Since we need only mode amplitudes $a(\boldsymbol{k})$, $a(\boldsymbol{p})$ and $a(-\boldsymbol{q})$ with wavevectors in $K^+$, then we need only compute the nonlinear terms $n(\boldsymbol{k}; \boldsymbol{p}, \boldsymbol{q}) = n(\boldsymbol{k}; \boldsymbol{q}, \boldsymbol{p})$, $n(\boldsymbol{p}; \boldsymbol{q}, \boldsymbol{k}) = n(\boldsymbol{p}; \boldsymbol{k}, \boldsymbol{q})$, and $n(-\boldsymbol{q}; -\boldsymbol{k}, -\boldsymbol{p}) = n(-\boldsymbol{q}; -\boldsymbol{p}, -\boldsymbol{k})$. Note that $n(\boldsymbol{q}; \boldsymbol{k}, \boldsymbol{p})$ is not needed because $\boldsymbol{q}$ is not in the computation domain $K^+$. However, its conjugate $n(-\boldsymbol{q}; -\boldsymbol{k}, -\boldsymbol{p})$ must be computed because $-\boldsymbol{q}$ is in $K^+$. Using (3.1) and the reality condition for $a(\boldsymbol{k})$, the nonlinear interactions $n(\boldsymbol{k}; \boldsymbol{p}, \boldsymbol{q})$ and $n(\boldsymbol{p}; \boldsymbol{q}, \boldsymbol{k})$ are computed as:

$$\left.\begin{array}{l} n(\boldsymbol{k}; \boldsymbol{p}, \boldsymbol{q}) = C_{kpq} a^*(\boldsymbol{p}) a(-\boldsymbol{q}), \\ n(\boldsymbol{p}; \boldsymbol{q}, \boldsymbol{k}) = C_{pqk} a(-\boldsymbol{q}) a^*(\boldsymbol{k}), \end{array}\right\} \quad (3.3)$$

where $a^*(\boldsymbol{q})$ is computed using $a(-\boldsymbol{q})$ since $\boldsymbol{q}$ is not in the computation domain $K^+$. Finally, $n(-\boldsymbol{q}; -\boldsymbol{k}, -\boldsymbol{p})$ is computed using reality of $C_{kpq}$ and the conjugate triad $\triangle_{-k,-p,-q}$:

$$n(-\boldsymbol{q}; -\boldsymbol{k}, -\boldsymbol{p}) = C_{qkp}a(\boldsymbol{k})a(\boldsymbol{p}). \qquad (3.4)$$

Again, amplitudes $a(\boldsymbol{k})$ and $a(\boldsymbol{p})$ with wavevectors in $K^+$ are used for amplitudes $a^*(-\boldsymbol{k})$ and $a^*(-\boldsymbol{p})$ with wavevectors in $K^-$, respectively. Expressions (3.3) and (3.4) are combined to compute the nonlinear interactions for the triad $\triangle_{kpq}$ and its conjugate triad $\triangle_{-k,-p,-q}$, using only modes with wavevectors in $K^+$ ($a(\boldsymbol{k})$, $a(\boldsymbol{p})$, and $a(-\boldsymbol{q})$).

It remains to discuss how to identify the triads in $T$, and it is enough to find the triads in $T \cap T^+$ because of the reality conditions. This requires a systematic procedure to search over all triads in $T^+$. For this purpose, an order is introduced between wavevectors in $K^+$:

$$\boldsymbol{k} < \boldsymbol{p} \quad \text{if either} \quad k_x < p_x, \quad \text{or} \quad k_x = p_x, k_y < p_y. \qquad (3.5)$$

Then, for each triad $\triangle_{kpq}$ in $T^+$ and without loss of generality, one can assume that $\boldsymbol{k}$ and $\boldsymbol{p}$ are in $K^+$ with $\boldsymbol{k} < \boldsymbol{p}$ and $\boldsymbol{q} = -\boldsymbol{k} - \boldsymbol{p}$ (e.g. see the triad in figure 1). The procedure to span $T^+$ is now straightforward: for each $\boldsymbol{k}$ in $K^+$, loop over all $\boldsymbol{p}$ in $K^+$ with $\boldsymbol{p} > \boldsymbol{k}$. If the triad $\triangle_{kpq}$ in $T^+$ is also an element of $T$, then store the triad and its interaction coefficients.

> for each $\boldsymbol{k} \in K^+$,
> > for each $\boldsymbol{p} \in K^+$ and $\boldsymbol{p} > \boldsymbol{k}$,
> > > Let $\boldsymbol{q} = -\boldsymbol{k} - \boldsymbol{p}$.
> > > > Check $\triangle_{k,p,q} \in T$.
> > > > > if yes, store $\triangle_{k,p,q}$ and its interaction coefficients
> > end of $\boldsymbol{p}$ for-loop
> end of $\boldsymbol{k}$ for-loop

Note that if $\boldsymbol{p} = \boldsymbol{k}$, then the triad $\triangle_{kpq}$ is collinear, and the nonlinear interactions among the triad are identically zero. Thus, it is sufficient to consider $\boldsymbol{p}$ which is strictly greater than $\boldsymbol{k}$.

## 4. Numerical results

The dimensional version of (2.1) with all nonlinear interactions in $\mathscr{I}_F$ or reduced model (2.9) is integrated forward in time using the third-order Runge–Kutta time-stepping scheme. For all calculations, the physical domain is a doubly periodic square with area $(2\pi)^2$, and the initial velocity is $\boldsymbol{u}(\boldsymbol{x}, t) = \boldsymbol{0}$. The linear wave and viscosity terms are treated using an integrating factor technique. The nonlinear term in the full simulations with $\mathscr{I}_F$ is calculated in physical space using FFTs, while the nonlinear interactions of reduced dynamics (2.9) are computed directly in Fourier space using the procedure discussed in §3.

Following Smith & Waleffe (1999), at times $t > 0$, a white noise force adds energy at an average rate $\varepsilon_f \approx 1$. The forcing spectrum $F(k)$ is Gaussian with peak wavenumber $k_f$ and standard deviation $\sigma = 1$, given by

$$F(k) = \varepsilon_f \frac{\exp(-0.5(k - k_f)^2/\sigma^2)}{(2\pi)^{1/2}\sigma}, \qquad (4.1)$$
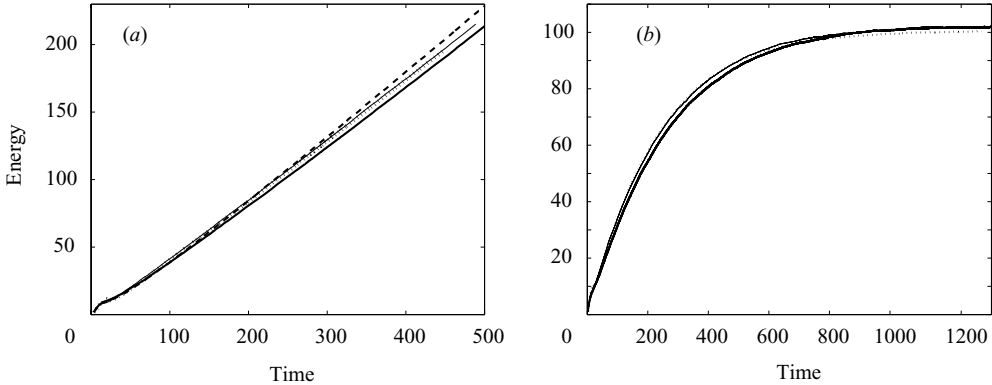
FIGURE 2. Total energy *vs.* time for $\beta$-plane flow with $Rh = 0.5$: (*a*) $\Lambda = 0$ and resolution $384^2$ Fourier modes; (*b*) $\Lambda = 2.2 \times 10^{-3}$ and resolution $256^2$. (*a, b*) Full simulation (thin solid line), near resonances with $\epsilon = 1$ (thick solid line), non-resonances with $\epsilon = 1$ (dotted line). (*a*) Near resonances with $\epsilon = 0.5$ (dashed line).

where $\varepsilon_f \approx 1$ is the energy input rate. With the forcing (4.1), the Rhines number is appropriately defined by

$$Rh = \frac{\left(\varepsilon_f k_f^5\right)^{1/3}}{\beta} \tag{4.2}$$

where the characteristic length is $L = 1/k_f$ and the nonlinear time scale is $L/U = (\varepsilon_f k_f^2)^{-1/3}$. The dissipation at small scales is modelled by a hyperviscosity term $-\nu_H \nabla^{2p_H}$ with $p_H = 8$ in place of the normal viscosity term $\nu \nabla^2$. The hyperviscosity is used to eliminate as far as possible the effects of viscosity at intermediate scales, thus extending the turbulence inertial range(s). We present runs with ($\Lambda \neq 0$) and without ($\Lambda = 0$) linear damping.

Many of the plots presented in the following sections are snapshots (at a single time) of energy spectra, vorticity and the zonally averaged profiles of velocity $u_{avg}(y)$, vorticity $\zeta_{avg}(y)$ and vorticity derivative $\zeta'_{avg}(y)$. On each plot of energy spectra, the spectrum $E(k)$ is the usual shell-integrated energy spectrum calculated by summing the energy of all modes with wavenumbers in $[k - \Delta k/2, k + \Delta k/2]$. The spectra $E_z(k_y)$ and $E_m(k_x)$ are the energy spectra corresponding to zonal and meridional flows, respectively, in a small sector $\pi/12$ about $k_x = 0$ and $k_y = 0$ (see also Chekhlov *et al.* 1996). On all plots, flow quantities are left dimensional with the exceptions of time and energy, which are scaled by $(\varepsilon_f k_f^2)^{-1/3}$ and $(\varepsilon_f / k_f)^{2/3}$, respectively.

### 4.1. *Developing flow on the $\beta$-plane*

We first consider flow on the $\beta$-plane given by (2.1) with $Rh = 0.5$ and $\Lambda = 0$. The resolution is $384^2$ Fourier modes, the forcing is in the range $67.5 < k < 82.5$ and the energy input rate is $\varepsilon_f \approx 1$. Figure 2(*a*) shows total energy *vs.* time for four different runs: (i) the full simulation with all triads $\mathscr{I}_F$ (thin solid); (ii) near resonances defined by (2.10) including the set of triads $\mathscr{I}_R(\epsilon = 1; Rh = 0.5)$ (thick solid); (iii) non-resonant triads $\mathscr{I}_N(\epsilon = 1; Rh = 0.5)$ (dotted line); and (iv) near-resonant triads $\mathscr{I}_R(\epsilon = 0.5; Rh = 0.5)$ (dashed line). In resolution $384^2$, the set $\mathscr{I}_R(\epsilon = 0.5; Rh = 0.5)$ contains about 18.6% of the full set of triad interactions $\mathscr{I}_F$, and the set $\mathscr{I}_R(\epsilon = 1; Rh = 0.5)$ contains about 33.6%. The percentage of the total triad interactions contained in any reduced model depends on the Rhines number, the value
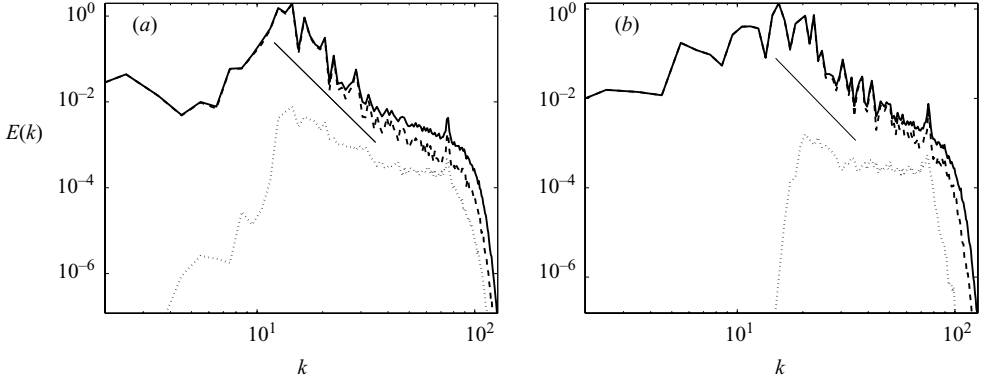
FIGURE 3. Energy spectra $E(k)$ (solid line), $E_z(k_y)$ (dashed line) and $E_m(k_x)$ for $Rh = 0.5$ at time $t = 350$: (*a*) full simulation; (*b*) near resonances with $\epsilon = 1$. In both plots, a $k^{-5}$ line is also shown for reference.
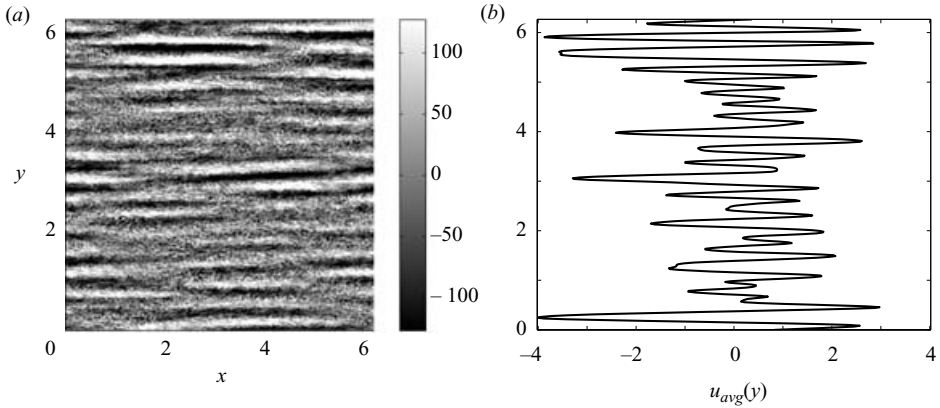


FIGURE 4. A full simulation of $\beta$-plane flow with $Rh = 0.5$ at time $t = 350$: (*a*) snapshot of vorticity; (*b*) zonally averaged velocity.

of $\epsilon$ and the resolution. Notice that, for non-dimensional times greater than about $t = 200$, the energy grows slightly faster with a subset of triads $\mathscr{I}_R(\epsilon = 0.5; Rh = 0.5)$ than with the full set of triads $\mathscr{I}_F$, indicating that the near resonances with $\epsilon = 0.5$ allow less leakage of energy to scales smaller than the forced scales. A similar phenomenon was observed for three-dimensional rotation, where enhanced energy transfer to large scales was observed for near resonances defined by values of $\epsilon$ less than one (Smith & Lee 2005). In general, the energy growth rates show only small differences for times less than $t \approx 500$, and so we have chosen to compare same-time snapshots of velocity and vorticity.

The time-developing characteristics of the full simulation are shown on figure 3(*a*) and figure 4 at non-dimensional time $t = 350$. Figures 3(*a*) and 4 show clearly that most of the energy input by the forcing is transferred to large-scale zonal flows with small $k_x$. Although we have drawn a $k^{-5}$ line on figure 3 for reference, the resolution is too low for the scaling to be convincing, at least for single-time spectra. Here we focus on other features that remain robust even in low resolution and for single-time snapshots. Figure 4(*b*) shows the bias of $u_{avg}(y)$ toward stronger westward velocities (see also figure 6). This bias is persistent throughout the time-developing
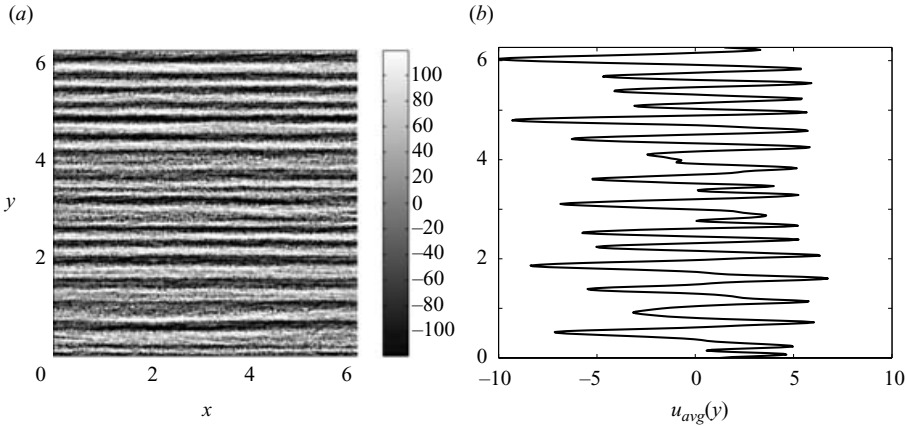
FIGURE 5. Near resonances with $\epsilon = 1$ and $Rh = 0.5$ at time $t = 350$: (*a*) snapshot of vorticity; (*b*) zonally averaged velocity.

flow when large-scale drag is unimportant. When large-scale damping is added and becomes dynamically important, then eastward jets strengthen and eventually become somewhat stronger on average than westward jets (see figure 9*a*).

The defining characteristics of the full simulation (at low resolution) with $Rh = 0.5$, in the absence of large-scale damping, are then (i) dominance of energy in large-scale zonal modes with small $k_x$, leading to $E(k) \approx E_z(k_y) \gg E_m(k_x)$ for wavenumbers sufficiently smaller than the forced wavenumbers, and (ii) a persistent bias toward stronger westward velocities (figure 6). Figure 3 shows that 'sufficiently smaller' means smaller than approximately $k_f/2$. These wavenumbers $k < k_f/2$ are also the wavenumbers exhibiting approximate scaling $E(k) \approx E_z(k_y) \propto k^{-5}$, albeit with large fluctuations.

The results at time $t = 350$ for a run retaining only near resonant triads with $\epsilon = 1$ and $Rh = 0.5$ are given in figures 3(*b*) and 5. Recall that $\epsilon$ is a parameter in (2.10), and here we have chosen the value $\epsilon = 1$ by analogy with the reduced-model calculations of three-dimensional rotating flows at moderate Rossby numbers $Ro \approx 0.1$ (Smith & Lee 2005). In figure 3(*b*), the spectra show strong dominance of zonal flows for $k < k_f/2$, indeed the ratio $E_z(k_y)/E_m(k_x)$ for $k_x = k_y < k_f/2$ is larger than for the full simulation. In figure 5(*b*), the asymmetry between eastward and westward jets is clear, with a bias toward stronger westward velocities. The asymmetry appears stronger than for the full simulation, since there are more westward jets with velocity greater than the maximum eastward velocity. Figure 6 shows the time evolution of the maximum eastward and maximum westward zonal velocities for both the full simulation and the run of near resonances with $\epsilon = 1$. For $t > 200$, the maximum westward velocity is always greater than the maximum eastward velocity in both flows, and both maxima are larger in the flow of near resonances than in the full $\beta$-plane flow. The stronger dominance of zonal flows, larger zonal velocities and stronger asymmetry are seen consistently during the time period $200 < t < 500$, while zonal flows are forming, but well before the peak energy has reached the smallest wavenumbers. In contrast, the complement set of non-resonant triad interactions with $\epsilon = 1$ does not lead to the formation of strongly zonal flows at large scales (figure 7).

The situation is similar to what was observed in three-dimensional homogenous rotation, where small-scale fluctuations self-organize into large-scale vortical columns, for both the full equations and near resonances with $\epsilon = 1$ (Smith & Lee 2005). For
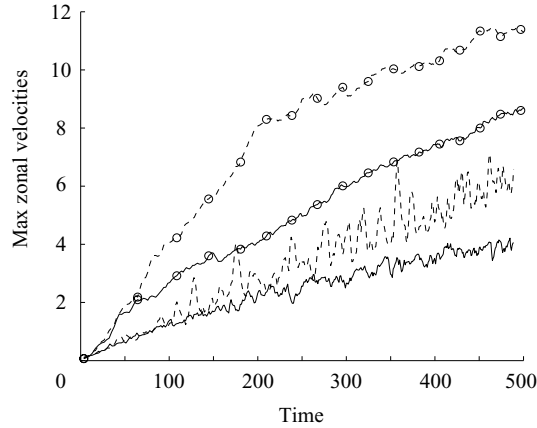
FIGURE 6. Maximum eastward (solid line) and westward (dashed line) velocities for flow with $Rh = 0.5$, $\Lambda = 0$ and resolution $384^2$: full simulation (lines without symbols); near resonances with $\epsilon = 1$ (lines with circles).
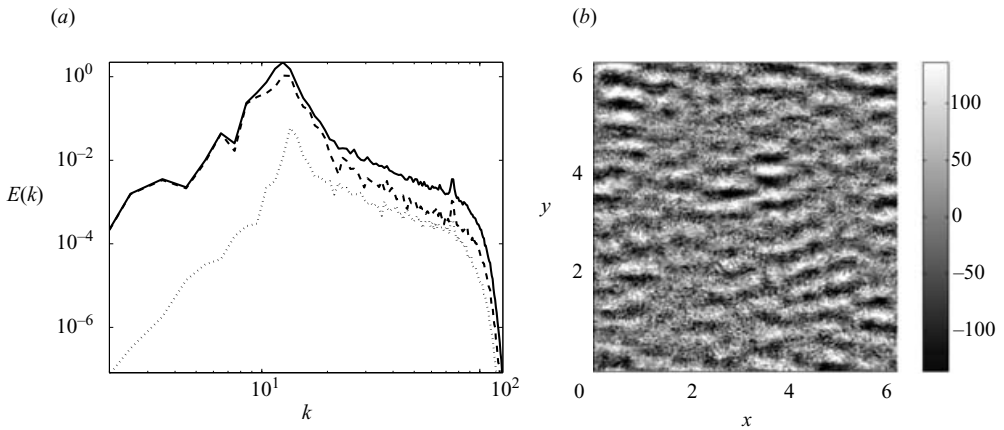


FIGURE 7. Non-resonances with $\epsilon = 1$ and $Rh = 0.5$ at time $t = 350$: (*a*) energy spectra $E(k)$ (solid line), $E_z(k_y)$ (dashed line), $E_m(k_x)$ (dotted line); (*b*) snapshot of vorticity.

both systems, there are more cyclones than anticyclones, and the maximum vorticities associated with cyclones are larger than those associated with anticyclones. In the flow of near resonances, the maximum vorticity within the cyclones was stronger than the maximum vorticity within the cyclones of the full simulation (see figure 14 in Smith & Lee 2005). Non-resonances with $\epsilon = 1$ did not generate large-scale vortical columns at all.

We have also explored different values of $\epsilon$ and of the Rhines number $Rh$. For near resonances in three-dimensional rotating flows at moderate Rossby numbers $Ro \approx 0.1$, the value $\epsilon = 0.3$ led to large-scale vortical columns, but without strong asymmetry in favour of cyclones (Smith & Lee 2005). Similarly, for near resonances on the $\beta$-plane at moderate Rhines numbers $Rh \approx 0.5$, we found that the value $\epsilon = 0.5$ led to strongly zonal flows, but the asymmetry in the amplitudes of eastward and westward jets was mostly lost. At time $t = 350$, we observed a large pile-up of energy at peak wavenumber $k = 25$, with smaller energy accumulation at $k = 50$ (recall that

the peak forcing wavenumber is $k_f = 75$). In contrast, at the same time $t = 350$ in the full simulation and in the simulation including near resonances with $\epsilon = 1$, the peak energy is at $k \approx 12$ (figure 3). Thus, for roughly the same total energy level and at the same time, interactions between near resonances with $\epsilon = 0.5$ lead to much thinner jets than observed in the full simulation and the reduced model of near resonances. Thus, we conclude that a value of $\epsilon$ closer to 1 is appropriate to define a reduced model of near resonances that captures essential flow features observed in the full simulation at moderate Rhines number $Rh = 0.5$.

The results for $Rh = 0.4$ with $\epsilon = 1$ are consistent with the results shown here for $Rh = 0.5$ with $\epsilon = 1$. For $Rh = 0.75$ with $\epsilon = 1$, the flow generated by near resonances is even more faithful to the full flow than for $Rh = 0.4$ and $Rh = 0.5$. One should keep in mind however, that for fixed resolution and fixed $\epsilon$, the percentage of the total triad interactions retained in the set of near resonances increases as the Rhines number increases. In the case of $Rh = 0.75$ with $\epsilon = 1$ at resolution $256^2$ Fourier modes, the near-resonant triads are about 46% of the total number of triads, and the reduction in the number of triads is much less than for $Rh = 0.4$ (28%) and $Rh = 0.5$ (33%). For $Rh > 1$, the concept of near-resonant triads ceases to be meaningful. The smallest value that we considered was $Rh = 0.1$, and again the near resonances with $\epsilon = 1$ closely mimic the full set of triads. We have not presented the results for $Rh = 0.1$ because the emergence of peaks in the spectrum $E(k)$ for the full simulation suggests that near resonances are not adequately resolved by our low resolutions ($512^2$ and lower) for $Rh = 0.1$. Recall that the reduced model calculations are necessarily fully spectral (rather than pseudospectral), and thus our comparisons between full and reduced models are restricted by time cost to low resolutions.

### 4.2. *Approach to a state of constant energy*

Figure 2(*b*) shows total energy as a function of time for runs with Rhines number $Rh = 0.5$ and non-dimensional drag coefficient $\Lambda = 2.2 \times 10^{-3}$. We can see that the flows are approaching a state of constant energy, and that the energy evolution is similar for the full simulation and the reduced models of near- and non-resonant triad interactions. We have chosen the time $t = 1000$ for the comparison of models to the full simulation, and note that flow characteristics at $t = 1000$ are representative of times $800 < t < 1200$.

Characteristics of the full simulation at $t = 1000$ are shown in figure 8. The spectra of figure 8(*a*) show clearly that large-scale zonal flows dominate large-scale meridional flows. The zonally averaged velocity $u_{avg}(y)$ in figure 8(*b*) has an asymmetry which is quite different from that observed in the time-developing case without drag shown in figure 4(*b*). Figure 9(*a*) (lines without symbols) shows that the westward jets are stronger for earlier times ($t < 700$) before the large-scale drag becomes important, as is consistent with the case without drag. Then, as the flow approaches a state of constant energy at later times ($t > 700$), the asymmetry between the eastward and westward jets is reversed, and the eastward jets become stronger and thinner than westward jets. Counting the number of strong jets with peak amplitude larger than a certain threshold (($2/3) \max |u_{avg}(y)|$ or $(3/4) \max |u_{avg}(y)|$), figure 9(*b*) (lines without symbols) shows that there are more strong eastward jets than westward jets after $t > 700$. Note that this crossover time, $t \approx 700$, is of the same order of magnitude as the time scale ($1/\Lambda \approx 454$) associated with the linear drag. The zonally averaged vorticity $\zeta_{avg}(y)$ in figure 8(*c*) exhibits the sawtooth pattern typical of constant-energy states with large-scale damping (e.g. Danilov & Gryanik 2004). The sawtooth pattern reflects thinner eastward jets and broader westward jets. The meridional derivative

(a)

(b)

(c)

(d)
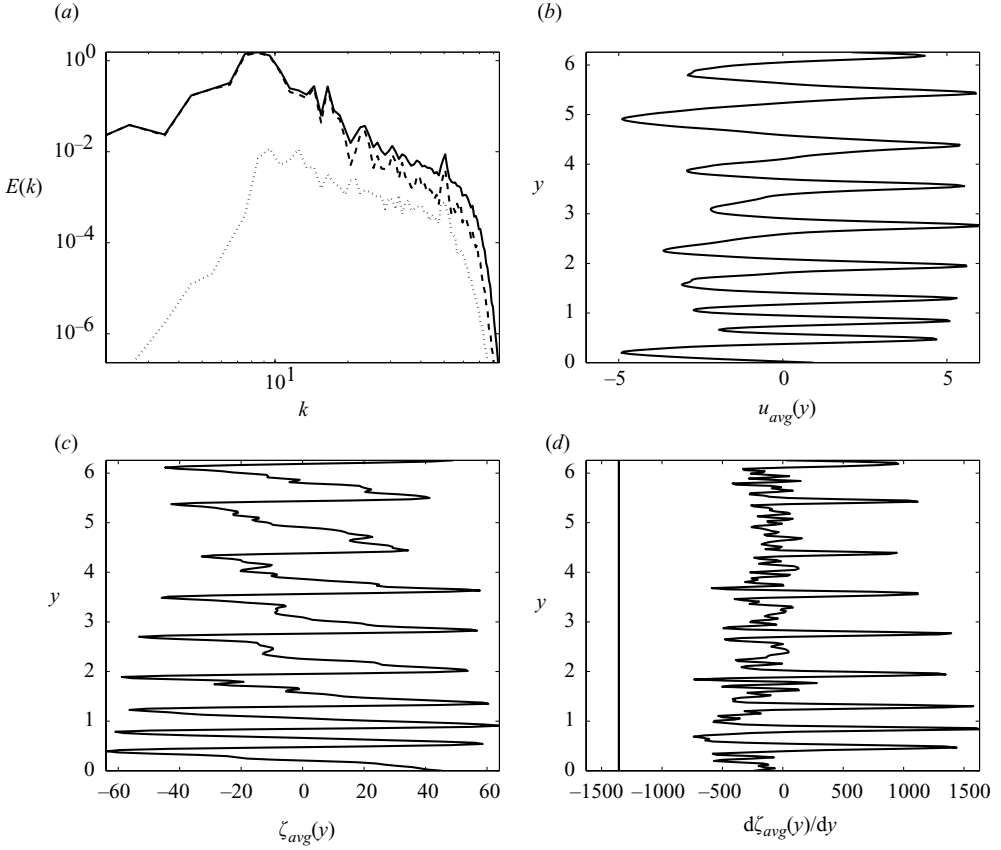
FIGURE 8. A full simulation with $Rh = 0.5$ and $\Lambda = 2.2 \times 10^{-3}$ at time $t = 1000$: (a) energy spectra $E(k)$ (solid line), $E_z(k_y)$ (dashed line), $E_m(k_x)$ (dotted line); (b) zonally averaged velocity; (c) zonally averaged vorticity; (d) meridional derivative of the zonally averaged vorticity, with the line $\zeta'_{avg}(y) = -\beta$ indicating the Rayleigh–Kuo condition.

$\zeta'_{avg}(y)$ of the zonally averaged vorticity in figure 8(d) is also strongly asymmetric with a distinctive signature. In figure 8(d), we have plotted the line $\zeta'_{avg}(y) = -\beta$, since by the Rayleigh–Kuo theorem, a necessary condition for linear instability of a zonal shear flow is that $\zeta'_{avg}(y) + \beta$ changes sign somewhere in the flow domain (see Kuo 1949, and also compare to figure 12c). The zonally averaged velocity profile corresponding to this nonlinear flow regime is stable in the linear sense.

Figure 10 shows energy spectra at time $t = 1000$ for the runs of near resonances (a) and non-resonances (b) with $\epsilon = 1$ and $Rh = 0.5$. As expected, the former (latter) is (is not) strongly zonal. As a measure of the average large-scale anisotropy, figure 11 shows the numerical approximation to the quantity

$$\text{ALSA} \equiv \frac{1}{k_f} \int_0^{k_f} \frac{E_z(k)}{E(k)} \mathrm{d}k \qquad (4.3)$$

where $k_f = 50$ is the peak wavenumber of the force, we compute the zonal spectrum $E_z(k)$ in a sector $\pi/12$ about $k_x = 0$, and ALSA stands for average large-scale anisotropy. In figure 11(a), the time evolution of ALSA is compared for the full simulation (solid line), near resonances (dashed line) and non-resonances (dash-dotted
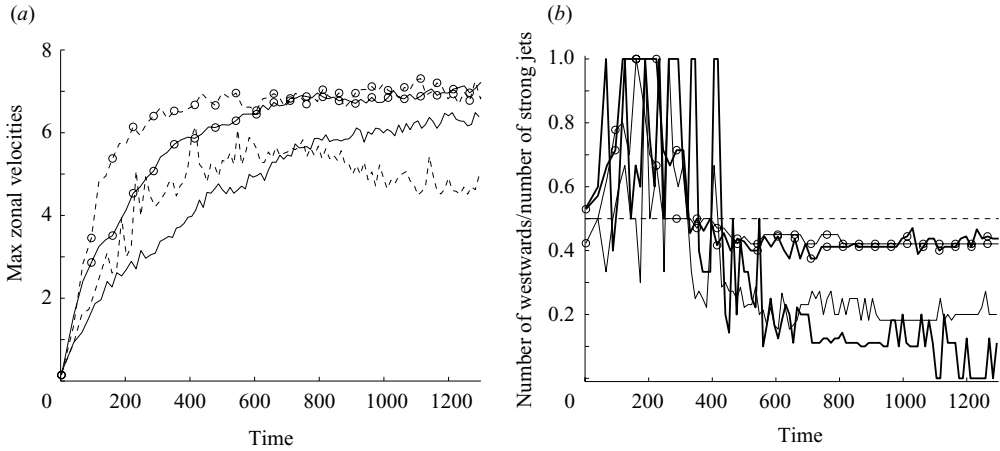
FIGURE 9. Comparison of flow quantities for the full simulation (lines without symbols) and the run of near resonances with $\epsilon = 1$ (lines with circles). Both flows have $Rh = 0.5$, $\Lambda = 2.2 \times 10^{-3}$ and resolution $256^2$: (a) maximum eastward (solid line) and westward (dashed line) velocites; (b) the ratio of the number of strong westward jets to the total number of strong jets. A jet is 'strong' if it has peak magnitude above $(2/3) \max |u_{avg}(y)|$ (thin lines) and $(3/4) \max |u_{avg}(y)|$ (thick lines). The dashed line indicates the ratio $1/2$, corresponding to an equal number of strong westward and strong eastward jets.
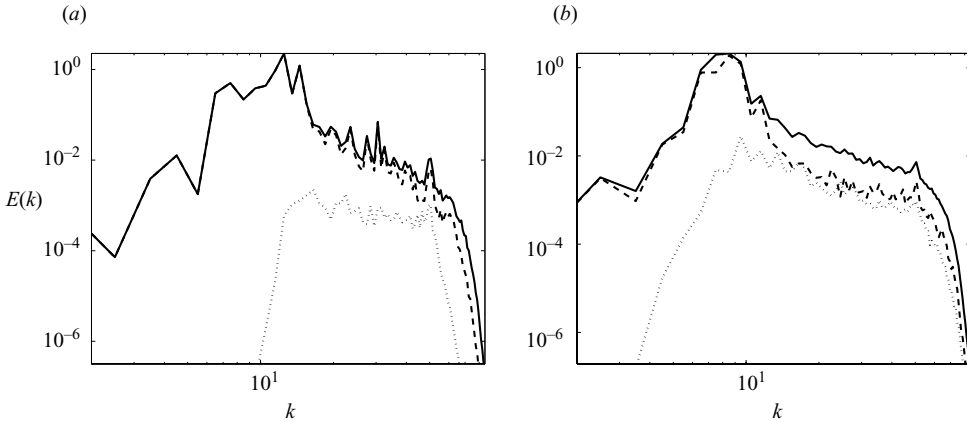


FIGURE 10. Energy spectra $E(k)$ (solid line), $E_z(k_y)$ (dashed line) and $E_m(k_x)$ (dotted line) for reduced models with $\epsilon = 1$, $Rh = 0.5$ and $\Lambda = 2.2 \times 10^{-3}$ at time $t = 1000$: (a) near resonances; (b) non-resonances.

line), all with $Rh = 0.5$. For times $t > 400$, we can see that the flow resulting from near-resonant interactions only is more perfectly zonal with ALSA $\approx 0.76$ compared to the full simulation with ALSA $\approx 0.6$, and compared to the flow resulting from non-resonances only with ALSA $\approx 0.35$.

Figure 11(b) shows how the average large-scale anisotropy increases as the Rhines number is decreased from $Rh = 5$ to $Rh = 0.4$ in numerical simulations with small-scale forcing in the range $45 < k < 55$, large-scale drag coefficient $\Lambda = 2.2 \times 10^{-3}$ and resolution $256^2$ Fourier modes. Taking a time average of the ALSA measure (4.3) for long times $t > 600$, figure 11(b) compares full simulation results (circles) to results for the reduced models of near resonances (stars) and non-resonances (crosses). In all
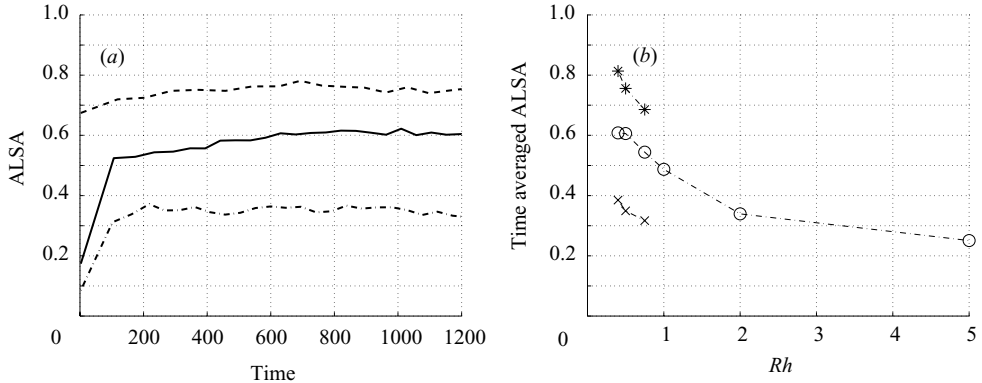
FIGURE 11. Average large-scale anisotropy ALSA as given by (4.3). All runs have $\Lambda = 2.2 \times 10^{-3}$. (a) ALSA *vs.* time for runs with $Rh = 0.5$: full simulation (solid line); near resonances with $\epsilon = 1$ (dashed line); non-resonances with $\epsilon = 1$ (dash-dotted line); (b) Time-averaged ALSA *vs.* $Rh$: full simulations (circles); near resonances with $\epsilon = 1$ (stars); non-resonances with $\epsilon = 1$ (crosses).

runs, the time average was computed for $t > 600$ until the end of the run: $t \approx 1000$ for runs of the full $\beta$-plane model with $Rh = 1, 2, 5$ and $t \approx 1300$ for other runs. Recall that the concept of near-resonant interactions is meaningful for $Rh < 1$, and that our resolution of $256^2$ Fourier modes appears to resolve near-resonant interactions adequately for a small range $0.1 < Rh < 1$. The resolution constraint applies to both the full and reduced models, and to be conservative, we present results only for $Rh \geqslant 0.4$. The open circles show that the large-scale anisotropy ratio for the full $\beta$-plane system increases from about 0.25 at $Rh = 5$ to about 0.61 at $Rh = 0.4$. Both reduced models show the same trend as the full simulation for the values $Rh = 0.75, 0.5, 0.4$, but the run of near (non) resonances is considerably more (less) zonal.

Figure 12 at time $t = 1000$ is representative of the zonal structure of the near-resonances flow with large-scale damping. Approaching the constant-energy state with near resonances only, the asymmetry between eastward and westward jets is weaker than for the full simulation. The maximum eastward and westward zonal velocities become almost the same after $t > 700$ (figure 12$a$ and lines with circles in figure 9$a$). However, figure 12($a$) shows that the peaks of the eastward jets are more uniformly large, whereas there are several westward jets with significantly lower amplitude. Counting the number of strong jets whose peak magnitudes are larger than $(2/3) \max |u_{avg}(y)|$ or $(3/4) \max |u_{avg}(y)|$, figure 9($b$) (lines with circles) indeed shows an asymmetry in favour of stronger eastward jets, although weaker than for the full simulation (lines without symbols). In figure 12($b$) showing a snapshot at time $t = 1000$ of the zonally averaged vorticity $\zeta_{avg}(y)$, the sawtooth pattern is also perceptible, but obscured by the presence of a secondary oscillation (higher-wavenumber structure) that is even more apparent when one focuses on a smaller portion of the flow. Figure 13 compares $u_{avg}(y)$ and $\zeta_{avg}(y)$ for the full simulation ($a$ and $b$) and the near-resonances run ($c$ and $d$) in the region $4 < y < 6$. In the profile $\zeta_{avg}(y)$ for near resonances, the positions of the secondary oscillations correspond to inflection points in $u_{avg}(y)$ (figure 13$d$), and also to a secondary peak in the energy spectra $E(k)$ and $E_z(k_y)$ intermediate between the large-scale damping wavenumber and the forcing wavenumbers (at $k \approx 30$, see figure 10$b$). The location of that peak probably depends on the value of the large-scale damping wavenumber (i.e. the
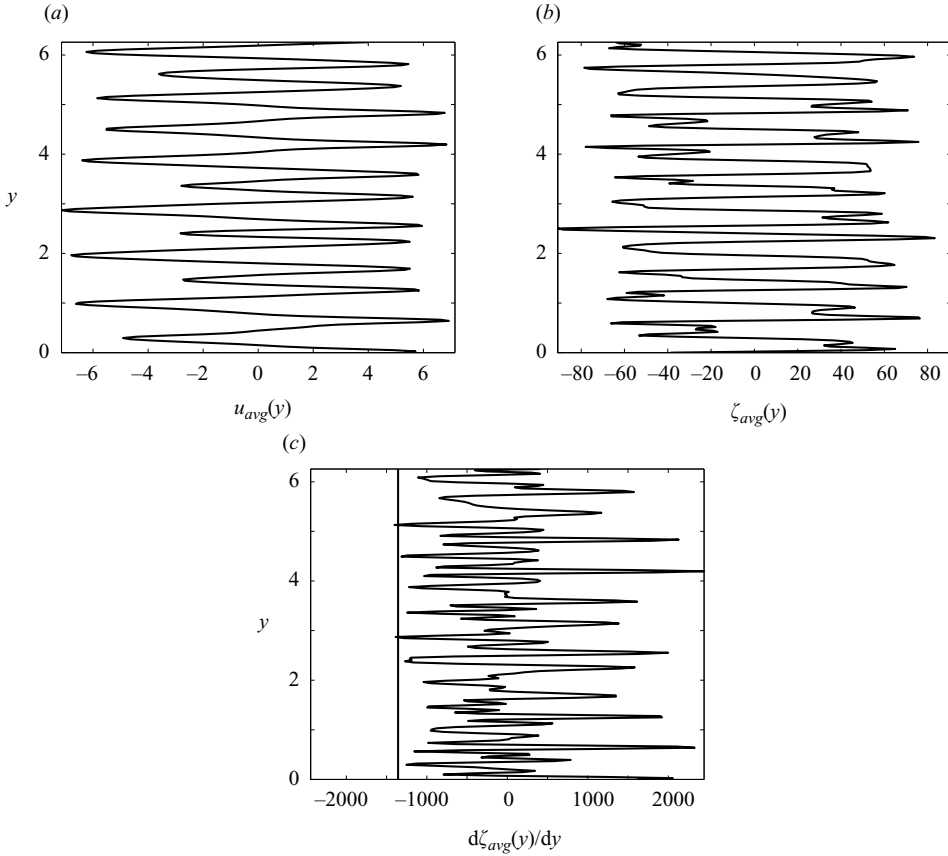
FIGURE 12. Near resonances with $\epsilon = 1$, $Rh = 0.5$ and $\Lambda = 2.2 \times 10^{-3}$ at time $t = 1000$: (a) zonally averaged velocity; (b) zonally averaged vorticity; (c) meridional derivative of the zonally averaged vorticity, with the line $\zeta'_{avg}(y) = -\beta$ indicating the Rayleigh–Kuo condition.

value of $\Lambda$) and the structure of the resonant traces (which are curves in the case of continuous wavenumber). Finally, turning attention to figure 12(c), we see that the signature of $\zeta'_{avg}(y)$ is altered as compared to the $\zeta'_{avg}(y)$ associated with the full simulation (figure 8d). The strong asymmetry in $\zeta'_{avg}(y)$ for the full simulation reflects the structure of the zonally averaged velocity, namely thinner eastward jets with amplitudes that are larger on average than those of westward jets, and the structure of the zonally averaged vorticity, namely the sawtooth pattern.

Figure 12(c) shows that the zonally averaged (mean) flow created by near resonances with small-scale forcing and large-scale damping reaches the Rayleigh–Kuo line $\zeta'(y) = -\beta$. Recall the Rayleigh–Kuo necessary condition for linear instability is that $\zeta'(y) + \beta$ changes sign somewhere in the flow domain. One interpretation is that nonlinear interactions generate a mean flow that is 'at best' marginally linearly stable (rather than linearly unstable, in which case those instabilities would presumably bring the mean back to marginal stability). However, the full set of nonlinear interactions generates a flow with zonal average that is well above the Rayleigh–Kuo line (figure 8d). Removing non-resonant interactions allows for development of a flow that (i) is more perfectly zonal, and (ii) has a zonal average that reaches the Rayleigh–Kuo line $\zeta'(y) = -\beta$ (figure 12c). Thus, the Rayleigh–Kuo condition appears
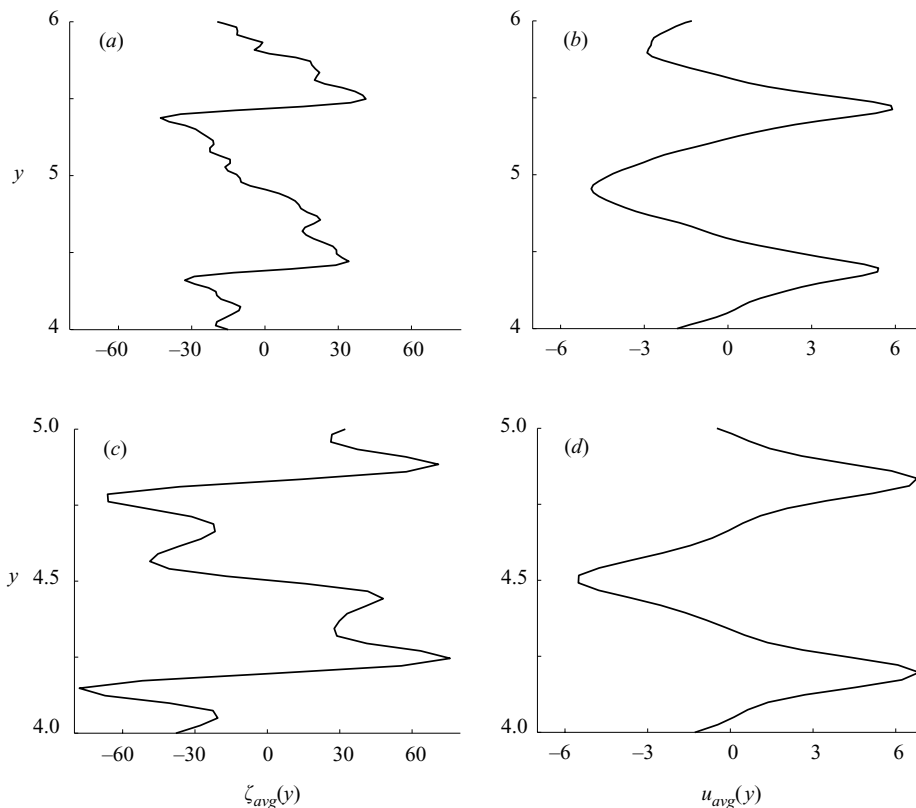
FIGURE 13. Close-up of $4 < y < 6$ for (a) zonally averaged vorticity and (b) zonally averaged velocity in the full simulation; (c) zonally averaged vorticity and (d) zonally averaged velocity in the run of near resonances with $\epsilon = 1$. In both runs, $Rh = 0.5$, $\Lambda = 2.2 \times 10^{-3}$ and $t = 1000$.

to be a relevant stability boundary for development of the flow in the reduced model of near-resonant interactions.

## 5. Conclusions and discussion

We have shown that simulations of near-resonant triads $\mathscr{I}_R(\epsilon; Rh)$ defined by (2.10) with $\epsilon = 1$ capture the main features of time-developing flow on the full $\beta$-plane at moderate Rhines numbers $Rh \approx 0.5$, with small-scale forcing and without large-scale damping. Those features are the generation of strongly zonal flows, and the persistent bias toward larger-amplitude westward velocities. In fact, the asymmetry between westward and eastward velocities, in favour of stronger westward flows, is enhanced by near resonances with $\epsilon = 1$. The asymmetry is vastly reduced for $\epsilon = 0.5$, although the large-scale flow remains strongly zonal. The situation is reminiscent of the results for three-dimensional homogeneous flow with constant background rotation rate, where near resonances with $\epsilon = 1$ capture the formation of large-scale cyclonic vortical columns from small-scale fluctuations (Smith & Lee 2005). In that case, the asymmetry between cyclones and anticyclones is stronger for near resonances with $\epsilon = 1$ than for the full simulation, but the asymmetry is lost as $\epsilon$ is decreased significantly below one (e.g. for $\epsilon = 0.3$). Therefore we conclude that the most appropriate definition of near resonances is (2.10) with $\epsilon = 1$.

For both three-dimensional rotation and two-dimensional flow on the $\beta$-plane studied here, simulations of near-resonant triad interactions mimic simulations of the full set of triad interactions during the time period when energy is transferred from the forcing wavenumbers $k \approx k_f$ to smaller wavenumbers $k < k_f/2$, and when there is not significant forward transfer from $k > k_f/2$ to $k \approx k_f$. When large-scale damping is introduced in our $\beta$-plane simulations, and such forward transfer is established, then the flow tends toward a state of constant energy. The full flow exhibits thinner eastward jets with larger amplitudes (on average) than for westward jets, leading to the sawtooth pattern in the zonally averaged vorticity. We find that near resonances alone generate a secondary peak in energy spectra corresponding to a secondary oscillation in the zonally averaged vorticity profile, obscuring the sawtooth pattern, and generally altering the characteristic signatures of the zonally averaged velocity, vorticity and vorticity derivative. Non-resonances with $|\sigma(\boldsymbol{k}) + \sigma(\boldsymbol{p}) + \sigma(\boldsymbol{q})| > Rh$ apparently act to suppress this secondary structure, although we cannot rule out the possibility that the secondary structure is an artefact of the low resolution achieved in this work. Non-resonances alone do not lead to strongly zonal flows, either with or without large-scale drag.

## REFERENCES

AFANASYEV, Y. & WELLS, J. 2005 Quasi-two-dimensional turbulence on the polar beta-plane: laboratory experiments. *Geophys. Astrophys. Fluid Dyn.* **99**, 1–17.

BALK, A. 1991 A new invariant for Rossby wave systems. *Phys. Lett.* A **155**, 20–24.

BALK, A. 2005 Angular distribution of Rossby wave energy. *Phys. Lett.* A **345**, 154–160.

BALK, A., NAZARENKO, S. & ZAKHAROV, V. 1991 New invariant for drift turbulence. *Phys. Lett.* A **152**, 276–280.

BAROUD, C., PLAPP, B., SWINNEY, H. & SHE, Z. 2003 Scaling in three-dimensional and quasi two-dimensional rotating turbulent flows. *Phys. Fluids* **15**, 2091–2104.

BOYD, J. 2001 *Chebyshev and Fourier Spectral Methods*, 2nd edn. Dover.

CANUTO, C., HUSSAINI, M., QUARTERONI, A. & ZANG, T. 1988 *Spectral Methods in Fluid Dynamics*. Springer.

CHEKHLOV, A., ORSZAG, S., GALPERIN, B., SUKORIANSKY, S. & STAROSELSKY, I. 1996 The effect of small-scale forcing on large-scale structures in two-dimensional flows. *Physica* D **98**, 321–334.

CONNAUGHTON, C., NAZARENKO, S. & PUSHKAREV, A. 2001 Discreteness and quasiresonances in weak turbulence of capillary waves. *Phys. Rev.* E **63**, 046306.

DANILOV, S. & GRYANIK, V. 2004 Barotropic beta-plane turbulence in a regime with strong zonal jets revisited. *J. Atmos. Sci.* **61**, 2283–2295.

DANILOV, S. & GURARIE, D. 2004 Scaling, spectra and zonal jets in beta-plane turbulence. *Phys. Fluids* **16**, 2592–2603.

GALPERIN, B., SUKORIANSKY, S. & HUANG, H. 2001 Universal $n^{-5}$ spectrum of zonal flows on giant planets. *Phys. Fluids* **13**, 1545–1548.

GIERASCH, P., INGERSOLL, A., BANFIELD, D. *et al.* 2000 Observation of moist convection in Jupiter's atmosphere. *Nature* **403**, 628–630.

HOLLOWAY, G. & HENDERSHOTT, M. 1977 Statistical closure for nonlinear Rossby waves. *J. Fluid Mech.* **82**, 747–765.

HOPFINGER, E., BROWAND, K. & GAGNE, Y. 1982 Turbulence and waves in a rotating tank. *J. Fluid Mech.* **125**, 505–534.

HUANG, H. & ROBINSON, W. 1998 Two-dimensional turbulence and persistent zonal jets ins a global barotropic model. *J. Atmos. Sci.* **55**, 611–632.

HUANG, H., GALPERIN, B. & SUKORIANSKY, S. 2001 Anisotropic spectra in two-dimensional turbulence on the surface of a rotating sphere. *Phys. Fluids* **13**, 225–240.

INGERSOLL, A., GIERASCH, P., BANFIELD, D. *et al.* 2000 Moist convection as an energy source for the large-scale motions in Jupiter's atmosphere. *Nature* **403**, 630–632.

KUO, H. 1949 Dynamic instability of two-dimensional nondivergent flow in a barotropic atmosphere. *J. Met.* **6**, 105–122.

LOLLINI, L. & GODEFERD, F. 1999 Direct numerical simulations of turbulence with confinement and rotation. *J. Fluid Mech.* **393**, 257–307.

LONGHETTO, A., MONTABONE, L., PROVENZALE, A., DIDELLE, H., GIRAUD, C., BERTONI, D. & FORZA, R. 2002 Coherent vortices in rotating flows: a laboratory view. *Il Nuovo Cimento* **25**, 233–249.

LONGUET-HIGGINS, M. & GILL, A. 1967 Resonant interactions between planetary waves. *Proc. R. Soc. Lond.* A **299**, 120–140.

MANFROI, A. & YOUNG, W. 2002 Stability of $\beta$-plane Kolmogorov flow. *Physica* D **162**, 208–232.

MARCUS, P., KUNDU, T. & LEE, C. 2000 Vortex dynamics and zonal flows. *Phys. Plasmas* **7**, 1630–1640.

NEWELL, A. 1969 Rossby wave packet interactions. *J. Fluid Mech.* **35**, 255–271.

NOZAWA, R. & YODEN, S. 1997 Formation of zonal band structure in forced two-dimensional turbulence on a rotating sphere. *Phys. Fluids* **9**, 2081–2093.

OKUNO, A. & MASUDA, A. 2003 Effect of horizontal divergence on the geostrophic turbulence on a beta-plane: suppression of the Rhines effect. *Phys. Fluids* **15**, 56–65.

PEDLOSKY, J. 1986 *Geophysical Fluid Dynamics*. Springer.

PUSHKAREV, A. & ZAKHAROV, V. 2000 Turbulence of capillary waves – theory and numerical simulation. *Physica* D **135**, 98–116.

REZNIK, G. & SOOMERE, T. 1983 On generalized spectra of weakly nonlinear Rossby waves. *Oceanology* **23**, 692–694.

RHINES, P. 1975 Waves and turbulence on a beta-plane. *J. Fluid Mech.* **69**, 417–443.

RHINES, P. 1979 Geostrophic turbulence. *Annu. Rev. Fluid Mech.* **11**, 401–441.

SALMON, R. 1998 *Lectures on Geophysical Fluid Dynamics*. Oxford University Press.

SMITH, K. S. 2004 A local model for planetary atmospheres forced by small-scale convection. *J. Atmos. Sci.* **61**, 1420–1433.

SMITH, L. 2001 Numerical study of two-dimensional stratified turbulence. *Advances in Wave Intercation and Turbulence* (ed. P. A. Milewski, L. M. Smith, F. Waleffe & E. G. Tabak). Am. Math. Soc. Providence, RI.

SMITH, L. & LEE, Y. 2005 On near resonances and symmetry breaking in forced rotating flows at moderate Rossby number. *J. Fluid Mech.* **535**, 111–142.

SMITH, L. & WALEFFE, F. 1999 Transfer of energy to two-dimensional large scales in forced, rotating three-dimensional turbulence. *Phys. Fluids* **11**, 1608–1622.

SMITH, L. & WALEFFE, F. 2002 Generation of slow, large scales in forced rotating, stratified turbulence. *J. Fluid Mech.* **451**, 145–168.

SMITH, L. & YAKHOT, V. 1994 Finite-size effects in forced two-dimensional turbulence. *J. Fluid Mech.* **274**, 115–138.

SOMMERIA, J., MEYERS, S. & SWINNEY, H. 1988 Laboratory simulation of Jupiter's great red spot. *Lett. Nature* **331**, 689–693.

SUKORIANSKY, S., GALPERIN, B. & DIKOVSKAYA, N. 2002 Universal spectrum of two-dimensional turbulence on a rotating sphere and some basic features of atmospheric circulation on giant planets. *Phys. Rev. Lett.* **89**, 124501.

VALLIS, G. & MALTRUD, M. 1993 Generation of mean flows and jets on a beta plane and over topography. *J. Phys. Oceanogr.* **23**, 1346–1362.

WILLIAMS, G. 1978 Planetary circulations: 1. Barotropic representation of Jovian and terrestrial turbulence. *J. Atmos. Sci.* **35**, 1399–1426.